Unveiling the Role of Counter-Anions in Transition Metal-Based Oxygen Evolution Electrocatalysts

Xiang Wang,[a,b] Xu Han,[c] Ruifeng Du,[a,b] Zhifu Liang,[a,c] Yong Zuo,[a,d] Pablo Guardia,[a] Junshan Li,[e] Jordi Llorca,[f] Jordi Arbiol,[c,g] Renji Zheng,*[h,i] Andreu Cabot*[a,g]

[a] Catalonia Institute for Energy Research (IREC), Sant Adrià de Besòs, 08930 Barcelona, Spain

[b] Departament d'Enginyeria Electrònica i Biomèdica, Universitat de Barcelona, 08028, Barcelona, Catalonia, Spain

[c] Catalan Institute of Nanoscience and Nanotechnology (ICN2), Campus UAB, Bellaterra, 08193 Barcelona, Catalonia, Spain

[d] Istituto Italiano di Tecnologia, Via Morego 30, 16163, Genova, Italy

[e] Institute of Advanced Study, Chengdu University, Chengdu 610106, China

[f] Institute of Energy Technologies, Department of Chemical Engineering and Barcelona Research Center in Multiscale Science and Engineering, Universitat Politècnica de Catalunya, EEBE, 08019, Barcelona, Catalonia, Spain

[g] ICREA, Pg. Lluis Companys, 08010 Barcelona, Catalonia, Spain

[h] School of Minerals Processing and Bioengineering, Central South University, Changsha 410083, China

[i] Key Laboratory of Hunan Province for Clean and Efficient Utilization of Strategic Calcium-containing Mineral Resources, Central South University, Changsha 410083, China

* E-mails: zhengrj@csu.edu.cn; A. Cabot: acabot@irec.cat;

Abstract

At the initial stage of the oxygen evolution reaction (OER) most electrocatalysts undergo a structural and chemical surface reconstruction. While this reconstruction strongly influences their performance, it is frequently overlooked. Herein, we analyze the role of the oxidized anions, which is particularly neglected in most previous works. We introduce a range of different anionic groups (Cl^-, CH_3COO^-, NO_3^-, SO_4^{2-}) on the surface of an amorphous $ZnCo_xNi_yO_z$ catalyst by a facile proton etching and ion exchange method from a ZIF-8 self-sacrificial

template. The structural and chemical properties of the obtained set of materials are thoroughly analysed and correlated with their electrocatalytic performance to study the effect of surface anionic groups, phase transition, metal leaching and defect generation on OER activity. Exploiting the control possibilities provided by the synthesis method here described and taking into account the uncovered property-performance correlations, the electrocatalyst is optimized. As a result, we produce $ZnCo_{1.25}Ni_{0.73}O_x$-SO_4 catalysts with outstanding OER performances, including a low overpotential of 252 mV at 10 mA cm^{-2} with a reduced Tafel slope of 41.6 mV dec^{-1}. Furthermore, this catalyst exhibits remarkable stability with negligible overpotential variation for 100 h. The excellent catalytic properties are rationalized using density functional theory calculations, showing that the surface-adsorbed anions, particularly SO_4^{2-}, can stabilize the OOH* intermediate, thus enhancing the OER activity.

Keywords: amorphous oxide, anion adsorption, structural reconstruction, leaching, oxygen evolution reaction.

1. Introduction

The electrochemical oxygen evolution reaction (OER) is a vital half-reaction in several renewable energy conversion and storage technologies. OER is coupled to hydrogen evolution in electrolyzers, a metal reduction in rechargeable metal-air batteries, nitrogen reduction to ammonia, and CO_2 reduction to methane or methanol for instance.[1-3] However, the slow kinetics of the involved multi-electron transfer processes severely reduce the OER activity.[4, 5] To address this crucial concern, a wide range of potential OER electrocatalysts have been developed. Among them, noble metal-free transition metal oxides,[6, 7] nitrides,[8, 9] phosphides,[10-12] and dichalcogenides[13, 14] are particularly interesting from a cost-effectiveness point of view. However, in-situ electrochemical analyses have frequently revealed that these compounds are not the real active material in the OER process, but they are inevitably oxidized and reconstructed into transition metal hydroxides ($M(OH)_x$) and oxyhydroxides (MOOH) during the first steps of the electrochemical reaction.[15-17] While several pieces of evidence of this transformation have been published, the fate and role within the electrochemical cell of the anions after the pre-catalyst is oxidized is rarely reported.

Besides, the extent of the transition metal transformation and the final metal reorganization and composition is hardly investigated. In particular, during the compound oxidation, it is very likely that some metal leaching occurs, which can also strongly affect the OER process.

During reconstruction, the surface anions are probably oxidized to nitrates (NO_3^-), phosphates (PO_4^{3-}), sulfates (SO_4^{2-}), or selenates (SeO_4^{2-}). In a few recent works, we and others have demonstrated the presence of such nonmetallic anionic groups to play a key role in the OER activity.[18-23]Accordingly, the rational design and engineering of catalysts containing controlled amounts of such anionic groups could be an effective strategy to improve their performance. In this direction, the introduction of anionic groups *a posteriori*, through surface adsorption, generally results in a weak chemical interaction that limits the effectiveness and stability of the resultant catalyst.[21] Thus, approaches for the direct incorporation of controlled amounts of anionic groups that enable a strong bonding between anions and metal atoms need to be developed.

On the other hand, amorphous catalysts generally display improved OER performance over their crystalline counterpart.[24, 25] Such catalysts present highly tunable atomic arrangement, compositions, and easier doping with a high concentration of extrinsic dopants.[26] Besides, amorphous oxides, also enable a larger range of metal oxidation states and result in higher concentrations of unsaturated coordination spheres.[27] Additionally, compared with crystalline materials, amorphous catalysts usually form less strong bonds with oxygen, which can facilitate an efficient lattice oxygen-mediated OER mechanism.[28, 29]

Beyond the abundant structural defects found in amorphous materials, the leaching of controlled amounts of the composing transition metal ions can *in situ* generate additional defects that may translate into active OER sites.[30-34]

Herein, we introduce different anionic groups (Cl^-, CH_3COO^-, NO_3^-, SO_4^{2-}) in $ZnCo_xNi_yO_z$ nanosheets by a facile proton etching and ion exchange method. We test the resulting materials for OER and study the material transformation during the reaction, including metal ion leaching. We thoroughly analyze the structural and chemical properties of the initial and evolved materials and correlate them with their electrocatalytic performance. Exploiting the control possibilities provided by the synthesis method and taking into account the uncovered property-performance correlations, the electrocatalyst is optimized to reach outstanding OER

performances. Additionally, the optimized catalyst is further studied using density functional theory (DFT) calculations, which allows for determining the influence of particular surface-adsorbed groups on the OER activity.

2. Material and methods

2.1. Chemicals

Zinc nitrate hexahydrate ($Zn(NO_3)_2 \cdot 6H_2O$), nickel nitrate hexahydrate ($Ni(NO_3)_2 \cdot 6H_2O$), nickel chloride hexahydrate ($NiCl_2 \cdot 6H_2O$, 98%), cobalt nitrate hexahydrate ($Co(NO_3)_2 \cdot 6H_2O$, 99.9%), cobalt chloride hexahydrate ($CoCl_2 \cdot 6H_2O$, 98%), cobalt acetate tetrahydrate ($Co(CH_3COO)_2$, 98%), nickel(II) acetate tetrahydrate ($Ni(CH_3COO)_2$, 98%), cobalt sulfate hexahydrate ($CoSO_4 \cdot 6H_2O$,99%), nickel sulfate hexahydrate ($NiSO_4 \cdot 6H_2O$, 99%), potassium hydroxide (KOH, 85%), and 2-methylimidazole ($C_4H_6N_2$, 99%) were purchased from Acros Organics. Iridium(IV) oxide (IrO_2, 99.9% metal basis) and Nafion (5 wt% in a mixture of low aliphatic alcohols and water) were obtained from Sigma-Aldrich. Methanol, ethanol and isopropanol were of analytical grade and obtained from various sources. Milli-Q water was obtained from a Purelab flex from Elga. All chemicals were used as received, without further purification.

2.2. Zeolitic imidazolate framework (ZIF-8) MOF

Among the different MOFs, we selected the ZIF-8 due to its high versatility and ease of synthesis. The synthesis of ZIF-8 was based on a previous procedure with modifications.[37] Typically, 0.87 g $Zn(NO_3)_2 \cdot 6H_2O$ was dissolved in 30 mL methanol. This solution was incorporated into a second methanol solution having 1.97 g 2-methylimidazole. The final mixture was kept at room temperature for 24 h. White precipitates were collected using a centrifuge, washed with methanol, and dried overnight at 60 □.

2.3. Synthesis of $ZnCo_xNi_yO_z$.

100 mg of ZIF-8 was sonicated in 20 mL of ethanol for redispersion. The obtained dispersion was added into a 100 mL water solution having 300 mg $CoSO_4 \cdot 6H_2O$ and 300 mg $NiSO_4 \cdot 6H_2O$. The final mixture was vigorously stirred at room temperature for 12 h. The product was centrifuged, washed with water, and freeze-dried. The obtained products were calcined in the muffle furnace at 350 □ for 2 hours under an air atmosphere. The final products were obtained

after natural cooling to room temperature and denoted as $ZnCo_xNi_yO_z$-SO_4. Besides, $ZnCo_xNi_yO_z$-NO_3, $ZnCo_xNi_yO_z$-OAc, and $ZnCo_xNi_yO_z$-Cl were obtained using the same method, but substituting sulfates with equal amounts of chlorides, acetates, and nitrates, respectively. As a reference material, ZnO nanoparticles were obtained by the direct calcination of ZIF-8. Besides, $ZnCo_xNi_yO_z$-SO_4 samples with different metal contents were obtained by adjusting the amount of cobalt and nickel salts added.

3. Results and discussion

3.1. Synthesis and characterizations of catalysts

Figure 1 illustrates the two-step approach used to produce $ZnCo_xNi_yO_z$ from a self-sacrificial ZIF-8 template (see details in the experimental section). In the first step, the Zn-based ZIF-8 MOF is reacted with Ni and Co salts (sulfates, nitrates, chlorides or acetates). In this process, the protons produced by the metal cation (Co^{2+}, Ni^{2+}) hydrolysis ($M^{2+} + 2H_2O = M(OH)_2 + 2H^+$) etch the ZIF-8, dissociating its polyhedron structure.[38, 39] At the same time, the cobalt and nickel ions partially replace zinc within the structure. Meanwhile, the salt anions (SO_4^{2-}, NO_3^-, Cl^-, OAC^-) are anchored to the material surface by exchange with the MOF organic ligands.

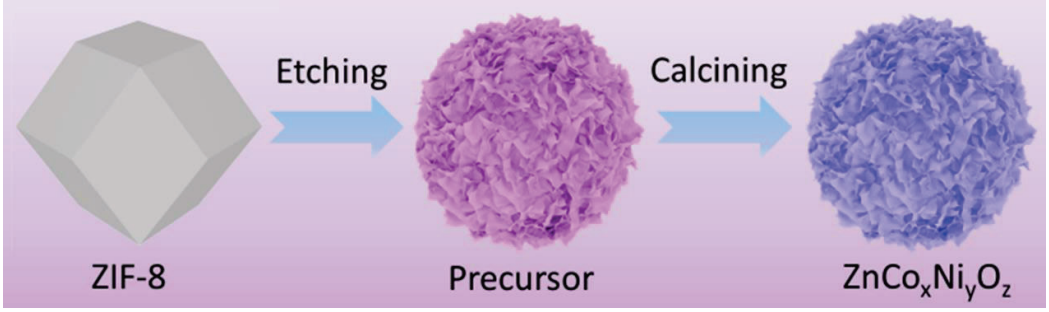

Figure 1. schematic illustration for the two-step preparation of $ZnCo_xNi_yO_z$ nanosheets from ZIF-8 MOF.

Figure 2a displays a representative SEM micrograph of the ZIF-8 particles, which were characterized by a dodecahedron shape and an average size of ca. 100 nm. Upon reaction with the transition metal sulfate, a nanosheet-like structure progressively expands around the gradually disappearing ZIF-8 template (Figure 2b). Eventually, the dodecahedron template has vanished and just the porous nanosheet structure is observed.

In the second step, the material is annealed under air to form an amorphous oxide. Figures 2c-e and S1 show SEM, TEM and STEM images of the ultrathin nanosheets with wrinkled

structures obtained after an annealing step at 350 °C in an air atmosphere. HRTEM analyses confirmed that the final $ZnCo_xNi_yO_z$-SO_4 presented an amorphous structure with no crystallographic ordering (Figure 2f,g). Meanwhile, HAADF-STEM and EELS compositional maps showed C, N, O, S, Zn, Co and Ni homogeneously dispersed within each nanosheet (Figures 2h and S2).

Figure 3a shows an AFM image of the $ZnCo_{1.26}Ni_{0.73}O_x$-SO_4 nanosheets. From the height line profiles of some of the nanosheets shown in Figure 3a, their average thickness was estimated at 1.7±0.2 nm (Figure 3b). From the N_2 adsorption-desorption isotherms displayed in Figure 3c, the Brunauer-Emmett-Teller (BET) surface area of $ZnCo_xNi_yO_z$-SO_4 was estimated at 93 m^2 g^{-1}, almost twice that of ZnO particles obtained from the annealing of ZIF-8 (49 m^2 g^{-1}). Additionally, the Barrett-Joyner-Halenda (BJH) average pore size and the integrated pore volume were 19.1 nm and 0.47 cm^3 g^{-1} for $ZnCo_xNi_yO_z$, and 18.1 nm and 0.16 cm^3 g^{-1} for ZnO particles. Such nanosheet morphology and mesoporous structure dramatically increase the percentage of surface unsaturated atoms, providing a high potential electroactive surface area, while facilitating the rapid diffusion of reactants and reaction products.

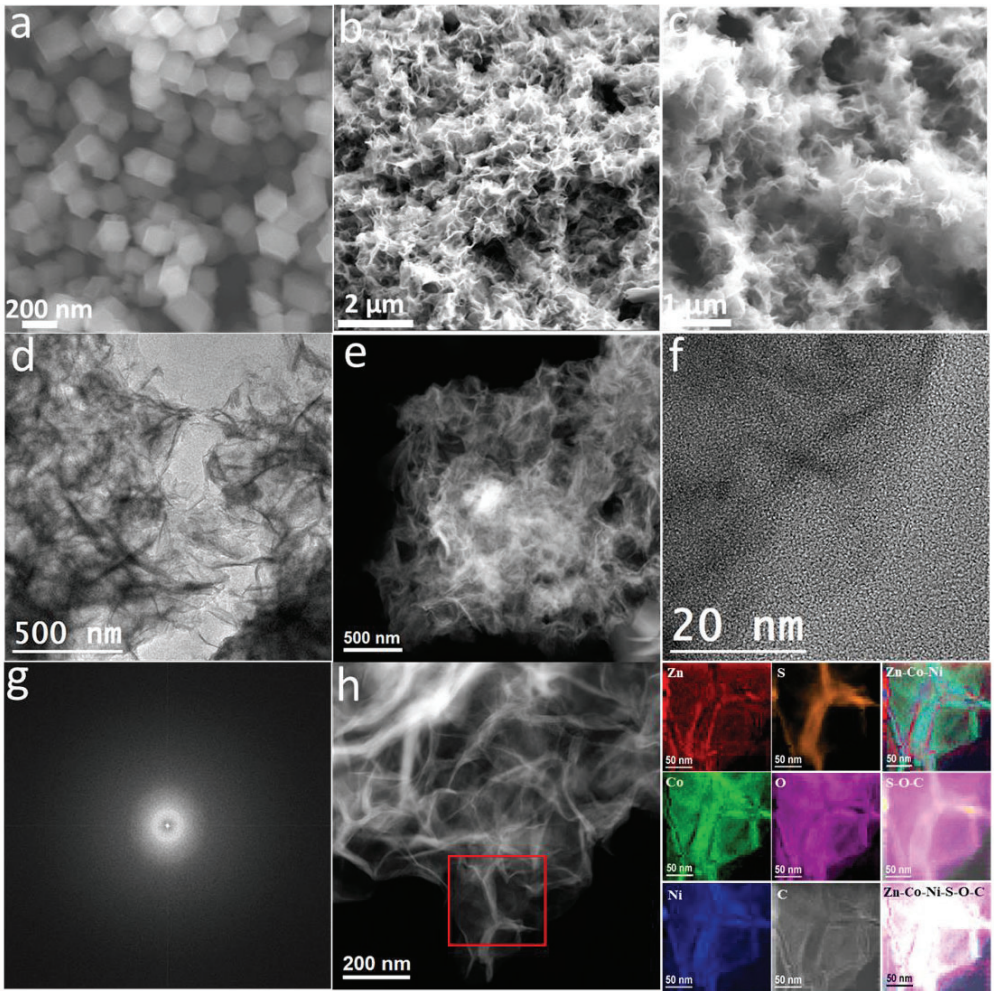

Figure 2. (a-c) SEM images of a) ZIF-8 MOF particles, b) $ZnCo_xNi_yO_z$-SO_4 precursor, and c) $ZnCo_xNi_yO_z$-SO_4 nanosheets. d) TEM image, e) HAADF STEM image, f) HRTEM image, g) corresponding power spectrum (FFT) and h) HAADF STEM images and EELS chemical composition maps of $ZnCo_xNi_yO_z$-SO_4 nanosheets. The EELS maps were obtained from the red squared area on the left HAADF STEM micrograph (left). Individual Zn $L_{2,3}$-edges at 1020 eV (red), Co $L_{2,3}$-edges at 779 eV (green), Ni $L_{2,3}$-edges at 855 eV (blue), S $L_{2,3}$-edges at 165 eV (orange), O K-edges at 532 eV (pink) and C K-edges at 285 eV (grey) and composites of Zn-Co-Ni, S-O-C and Zn-Co-Ni-S-O-C.

Figure 3d displays the FTIR spectra of $ZnCo_xNi_yO_z$ samples with different anions. $ZnCo_xNi_yO_z$-SO_4 displayed an evident FTIR absorption peak at about 600 cm^{-1}, which is a fingerprint of the presence of SO_4^{2-} ions.[40] The peaks at about 400, 550, and 640 cm^{-1} can be assigned to nitrate, chloride, and acetate, respectively.[41] The anionic groups played an important role in determining the crystallinity, morphology and composition of the obtained material, as evidenced by XRD, SEM and EDX analysis of $ZnCo_xNi_yO_z$ obtained with the different precursors (Figures 3e and S3-6). Because protons react with the surface of ZIF-8, breaking the coordinative bond between Zn^{2+} and 2-methylimidazole linkers in the ZIF-8, thus etching the

MOF and releasing Zn^{2+} ions into the solution,[37] we hypothesize that the crystallinity and architecture dependence on the used anion may be related to a different pH resulting from the hydrolysis of the different anions. To confirm this hypothesis, the pH of the solutions obtained from the dissolution of the same amount of different anionic metal salts was determined. The smallest pH value was obtained with the SO_4^{2-} (4.36) and increased in the following order: NO_3^-(5.75), Cl^-(7.02), and OAC^-(7.82). Such different pH values strongly determine the extent of MOF etching, thus affecting the crystallinity, morphology and also composition of the products. We observed that the lower the pH value, the weaker the crystallinity, the more favorable formation of nanosheets, and the lower Zn content on the final material.

In the same direction, the salt concentration also played an important role. Figures 3f and S7-9 show the XRD patterns, SEM images and EDX spectra of $ZnCo_xNi_yO_z$-SO_4 obtained using different concentrations of Ni and Co sulfates. When increasing the metal salt concentration, deeper hydrolysis and etching take place, which translates into a more amorphous structure, a more favorable nanosheet growth and a lower Zn content.

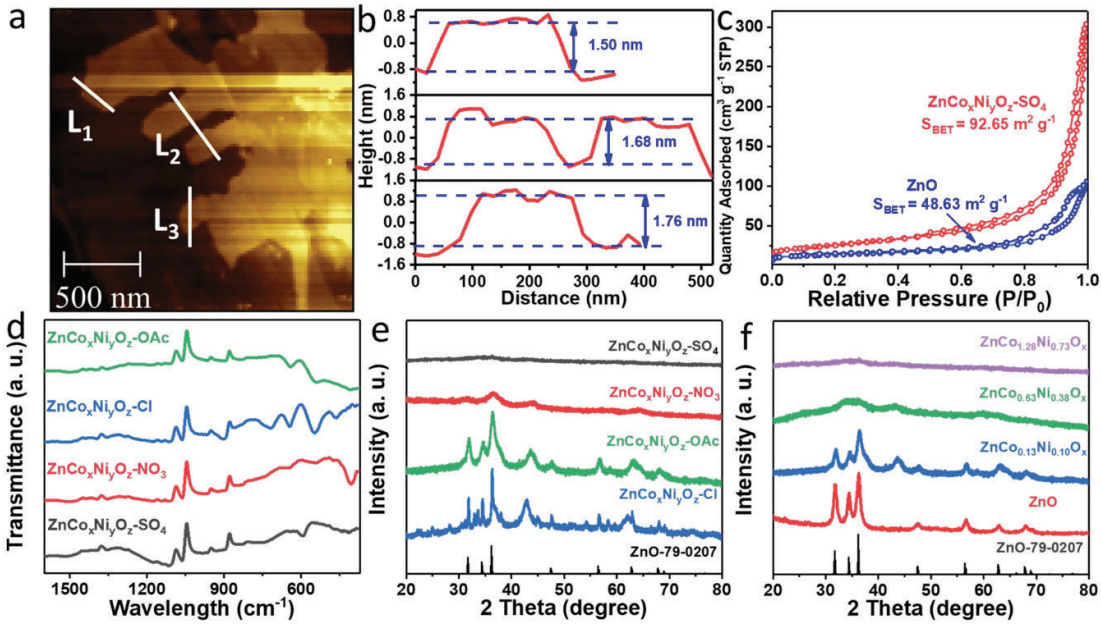

Figure 3. a) AFM images and b) the corresponding thickness measurement data of $ZnCo_{1.26}Ni_{0.73}O_x$-SO_4 Nanosheets. c) N_2 adsorption-desorption isotherms for $ZnCo_{1.26}Ni_{0.73}O_x$-SO_4 and ZnO. d) FTIR spectra and e) XRD patterns of $ZnCo_xNi_yO_z$ obtained from different anions. f) XRD pattern of $ZnCo_xNi_yO_z$-SO_4 with different metal content.

3.2. OER performance

The OER activity of $ZnCo_xNi_yO_z$ modified with different anions was initially assessed using LSV with a conventional three-electrode set-up in a 1 M KOH electrolyte. A commercial IrO_2 electrocatalyst was also tested as a reference. As shown in Figure 4a, the iR-compensated LSV curve of $ZnCo_xNi_yO_z$-SO_4 showed a very small overpotential at 10 mA cm^{-2} (η^{10}), just 252 mV, well below that of $ZnCo_xNi_yO_z$-NO_3 (287 mV), $ZnCo_xNi_yO_z$-Cl (314 mV), $ZnCo_xNi_yO_z$-OAc (348 mV) and IrO_2 (323 mV). The significant differences in overpotential demonstrate the important role played by the metal precursor counterions. Besides, by modifying the cobalt and nickel content, we determined the best OER performance to be obtained with a $ZnCo_{1.26}Ni_{0.73}O_x$-SO_4 composition (Figure 4b). In contrast, the ZnO produced from the annealing of the ZIF-8 was characterized by a much poorer performance with a η^{10} of 407 mV at 10 mA cm^{-2}.

Figure 4c displays the Tafel plots of the different catalysts. The $ZnCo_{1.26}Ni_{0.73}O_x$-SO_4 exhibited the smallest Tafel slope (41.6 mV dec^{-1}) among all the tested catalysts, including commercial IrO_2, thus demonstrating the fastest reaction kinetics. $ZnCo_{1.26}Ni_{0.73}O_x$-SO_4 also exhibited outstanding OER activity and kinetics when compared to some previously reported oxide-based OER electrocatalysts (Figure 4d and Table S4).

The ECSA was estimated from the double-layer capacitance (C_{dl}) measured by CV at different scanning rates (Figure S9 a-e). C_{dl} was calculated from the slope of the linear fitting of the charge current versus the scan rate (Figure 4e, Table S3).[27, 42] Using a specific capacity of 0.04 mF cm^{-2}, ECSA was estimated at 288 cm^2 for $ZnCo_{1.26}Ni_{0.73}O_x$-SO_4, well above that of the other catalysts evaluated (Table S2).[43] Figure 5f displays the specific activity obtained by normalizing the current to the ECSA. Despite its much larger ECSA, $ZnCo_{1.26}Ni_{0.73}O_x$-SO_4 also displayed the highest specific activity. We hypothesize this excellent activity to be related to a combination of different parameters, including a proper Zn/Co/Ni ratio, the presence of sulfate ions at the catalyst surface, its amorphous structure and its highly porous nanosheet-based architecture.

EIS was used to measure the interface charge transfer rate.[44] The charge transfer resistance (R_{ct}) of $ZnCo_{1.26}Ni_{0.73}O_x$-SO_4 was lower than those of the other samples (Fig. 4g), pointing at a faster charge transfer rate, in good agreement with the smallest Tafel slope.

Figure 4h shows the LSV curves of $ZnCo_xNi_yO_z$-SO_4 after 1000 and 5000 CV cycles. The overpotential needed to catalyze water oxidation at 10 mA cm^{-2} after 1000 and 5000 cycles test was virtually the same.

Figure 4h shows the initial LSV curve and the LSV profiles of $ZnCo_xNi_yO_z$-SO_4 after 1000 and 5000 CV cycles. The overpotential needed to catalyze water oxidation at 10 mA cm^{-2} after 1000 and 5000 cycles test was virtually the same. This overpotential was much lower than that displayed on the first LSV curve. The chronoamperometry (i-t) durability test for $ZnCo_xNi_yO_z$-SO_4 at the initial overpotential, showed a relatively stable and even increasing current density during 100 h of continuous operation (Figure 4i), indicating that the $ZnCo_{1.26}Ni_{0.73}O_z$-SO_4 electrocatalysts have excellent stability under the electrochemical conditions of water oxidation.

We hypothesize the overpotential decrease during the first cycles and the gradual increase of current density measured in the chronoamperometry test to be associated with progressive leaching of zinc ions. To test this hypothesis, the dissolution rate of different elements was monitored by analyzing the metal content within the electrolyte using ICP-MS. As shown in Figure S11f, negligible amounts of Co and Ni were dissolved during the 18 h chronoamperometric test. In contrast, a significant increase in the Zn concentration was detected within the electrolyte during the first 12 h of the reaction. The leaching of Zn initially generates metal vacancies and active sites within the reconstituted electrocatalyst, which can promote the OER performance.[34]

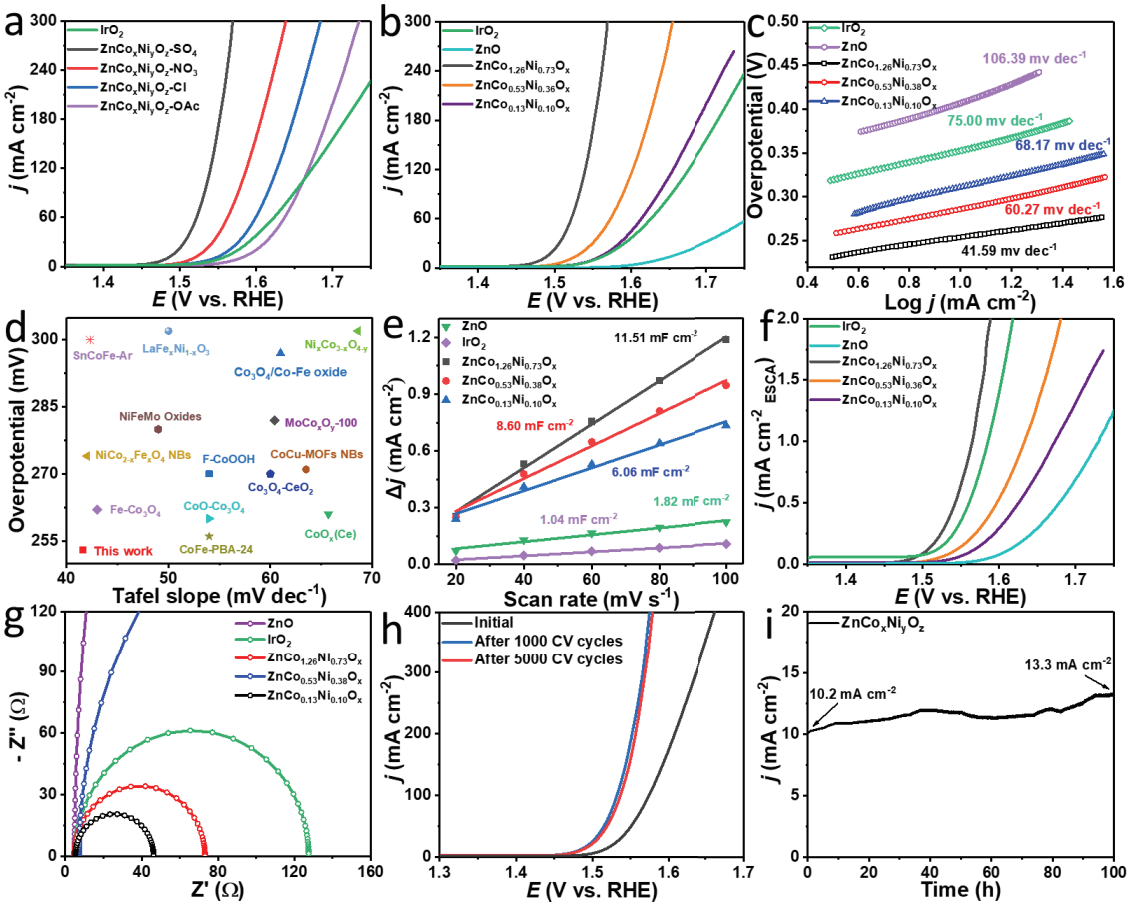

Figure 4. Electrocatalytic OER performance of the various catalysts. a-b) LSV curves of $ZnCo_xNi_yO_z$-M and $ZnCo_xNi_yO_z$-SO_4. c) Tafel plots. d) Comparison of overpotential at 10 mA cm^{-2} and Tafel slopes for $ZnCo_{1.26}Ni_{0.73}O_x$–SO_4 and some cobalt-based OER catalysts (Table S6). e) Capacitive current density measured at 1.17 V vs. RHE plotted as a function of scan rate. f) ECSA-normalized OER polarization curves. g) Nyquist plots at the potential of 1.52 V vs. RHE. h) LSV curves of $ZnCo_{1.26}Ni_{0.73}O_x$–SO_4 after 1000 and 5000 cycles. i) chronoamperometry curve of $ZnCo_{1.26}Ni_{0.73}O_x$–SO_4.

3.3. Structural and chemical evolution

To further reveal the parameters behind the excellent OER catalytic activity, the surface composition and chemical states of $ZnCo_{1.26}Ni_{0.73}O_z$-SO_4 before and after the OER test were characterized by XPS (Figure 5). The high-resolution O 1s XPS spectra of $ZnCo_{1.26}Ni_{0.73}O_z$-SO_4 showed the OER test to result in a negative shift of the lattice oxygen (O_L) signal located at 529.7 eV (Figure 5a). We associate this shift with the formation of surface metal (oxy)hydroxide that increases the electron density around the lattice O.[45, 46] [47] In addition, the O 1s peak at 531.5 eV, associated with surface hydroxide (OH_L), negatively shifted by 0.35 eV after the OER test. The OH_L/O_L ratio in the post-OER catalyst (2.50) was significantly higher than that in

the pristine $ZnCo_{1.26}Ni_{0.73}O_z$-SO_4 (2.03).[16] Interestingly, a clear S 2p XPS signal associated with sulfur within a sulfate chemical environment (S $2p_{3/2}$ = 168.7 eV) was measured both before and after the OER test. Besides the satellite peaks, two Co components were observed in the Co 2p spectra, and both also shifted to lower binding energies after the OER, from 780.7 eV to 780.5 eV for Co^{2+} (Co $2p_{3/2}$) and from 782.4 eV to 782.1 eV for the Co^{3+} (Co $2p_{3/2}$) component (Figure 5c). Additionally, the ratio Co^{3+}/Co^{2+} increased after the OER, from 1.1 to 1.5, indicating the formation of additional CoOOH species on the surface.[32] In the Ni 2p spectrum in Figure 5d, the Ni $2p_{3/2}$ peak was deconvoluted into two main peaks at 855.7 and 857.6 eV corresponding to Ni^{2+} and Ni^{3+}.[40] After OER, the Ni $2p_{3/2}$ peaks had shifted about 0.6 eV. Besides, the proportion of Ni^{3+} on the surface greatly increased from 36% to 49%. This result implies the transition of nickel species from oxides to (oxy)hydroxide.[48] Notably, the XPS signals of Zn became weak with the OER, consistent with the Zn leaching in an alkaline medium observed by ICP-MS.[48] This Zn leaching can favor the conversion of cobalt and Ni oxide on the surface of $ZnCo_xNi_yO_z$ to $CoO_x(OH)_y$ and $NiO_x(OH)_y$ species.[49, 50] Overall, XPS results confirmed the surface reconstruction of $ZnCo_{1.26}Ni_{0.73}O_z$-SO_4 during OER, chemically evolving from a surface metal oxide to metal (oxy)hydroxide species and loosing Zn during the process.[51]

The EPR spectra of $ZnCo_{1.23}Ni_{0.73}O_x$-SO_4 before and after OER were measured to explore species with unpaired electrons (Figure 5f).[52, 53] We observed the signal at g = 2.12, associated with the presence of oxygen vacancies V_o, to be strongly enhanced after OER test. Thus, a large density of oxygen vacancies was generated during OER, which is potentially associated with the zinc leaching, and which can favor the OER catalytic activity by introducing higher energy dangling bonds at the catalyst surface.[54, 55]

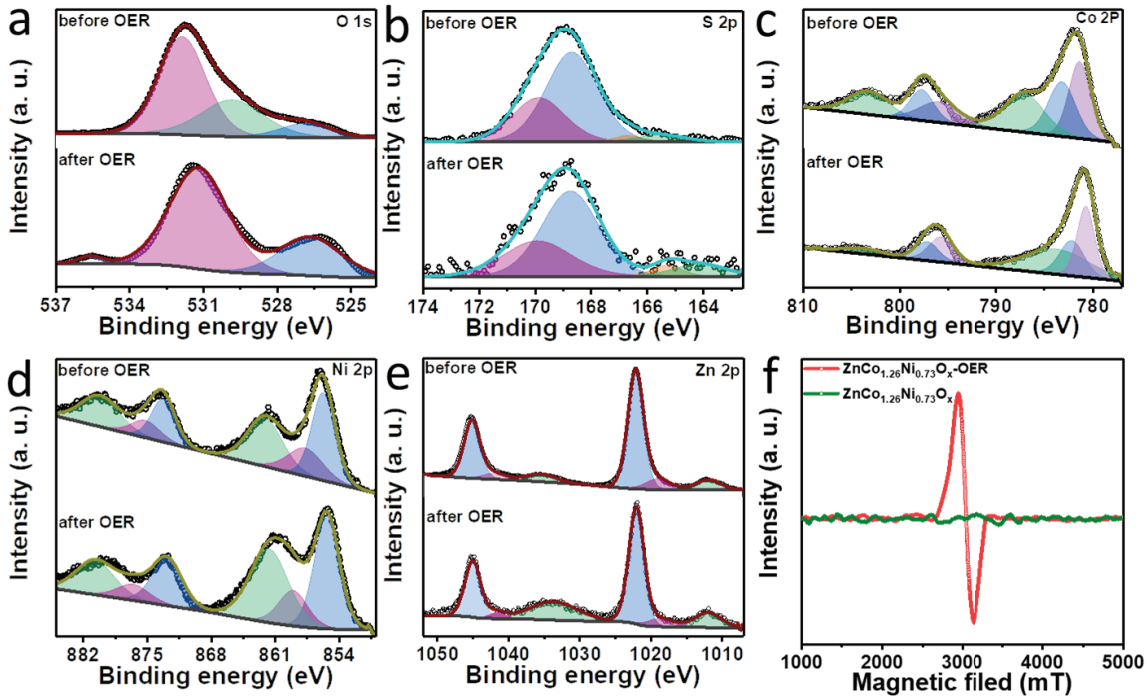

Figure 5. a-e) O 1s, S 2p, Co 2p, Ni 2p and Zn 2p high resolution XPS spectra. f) EPR spectrum of $ZnCo_{1.26}Ni_{0.73}O_x$-SO_4 before and after OER.

After OER, XRD and HRTEM analysis of $ZnCo_{1.26}Ni_{0.73}O_z$-SO_4 displayed the presence of the CoOOH crystal phase, formed during OER (Figure 6a-c). In contrast, electron microscopy images showed the nanosheet morphology to be preserved during the OER test. EELS elemental maps and HAADF-STEM images (Fig. 6d-e) showed a homogeneous dispersion of O, S, Zn, Co, and Ni in the cycled material. Besides, the comparison of the $ZnCo_{1.26}Ni_{0.73}O_z$-SO_4 composition before and after OER, as determined by EDX, ICP-MS and XPS analyses, showed a strong decrease in the amount of Zinc (Table S3).

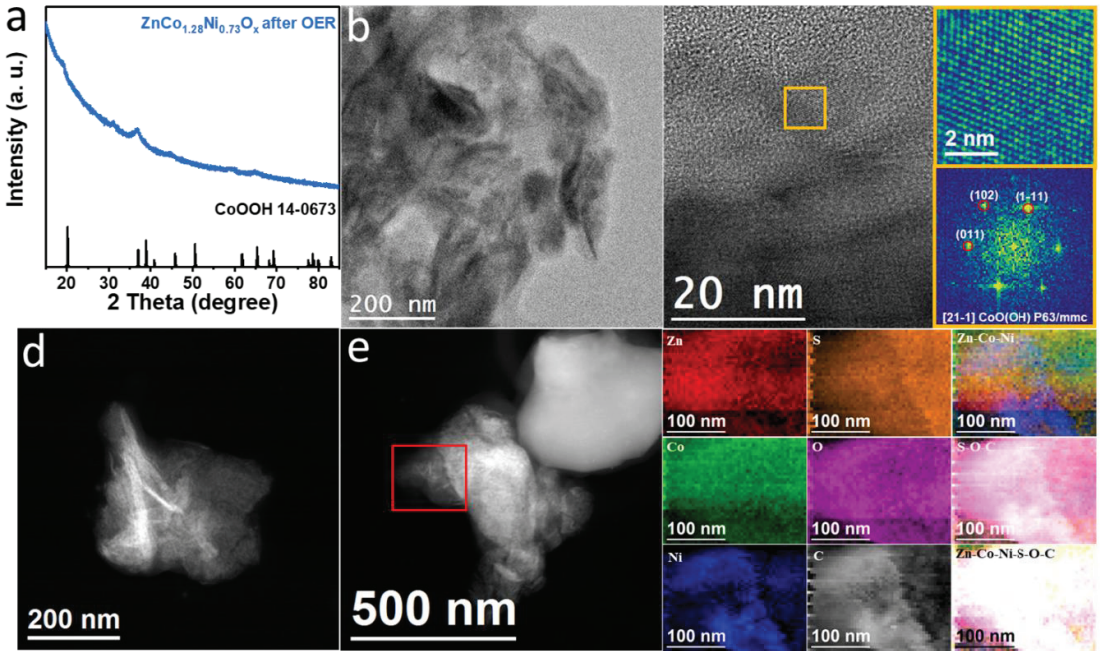

Figure 6. a) XRD pattern, b) TEM images, c) HRTEM and corresponding power spectrum (FFT), d) HAADF STEM image and e) HADDF EELS image together with the corresponding EELS chemical composition maps of $ZnCo_{1.26}Ni_{0.73}O_x$–SO_4 after OER. The EELS maps were obtained from the red squared area on the left HAADF STEM micrograph. Individual Zn $L_{2,3}$-edges at 1020 eV (red), Co $L_{2,3}$-edges at 779 eV (green), Ni $L_{2,3}$-edges at 855 eV (blue), S $L_{2,3}$-edges at 165 eV (orange), O K-edges at 532 eV (pink) and C K-edges at 284 eV (grey) and composites of Zn-Co-Ni, S-O-C and Zn-Co-Ni-S-O-C.

3.4. DFT calculations

DFT calculations were carried out to better understand the role of surface SO_4^{2-} on the enhancement of the OER activity. Owing to the complexity of the $ZnCo_{1.23}Ni_{0.73}O_x$-SO_4^{2-} amorphous structure, we used a cobalt oxohydroxide surface as a model system. First, we determined the CoOOH and CoOOH-SO_4 OER active sites. Besides the charge density and density of state (DOS) were calculated. Figures 7a and S11a show the optimized structural models of CoOOH-SO_4 and CoOOH for different OER steps. As displayed in Figure 7b, with the adsorption of the SO_4^{2-}, the contribution of the Co 3d orbital to the DOS at the Fermi level strongly increases.[20, 56]

The Gibbs free energies of OER pathways on CoOOH-SO_4 and CoOOH are displayed in Figures 6b and S11b,c. The formation of OOH* was determined to be the rate-determining step (RDS) on CoOOH. In the presence of the sulfate ion, CoOOH-SO_4 displayed a much lower free energy for OOH* generation when compared with CoOOH, which is consistent with the higher OER

activity experimentally measured for this material.[18, 57]

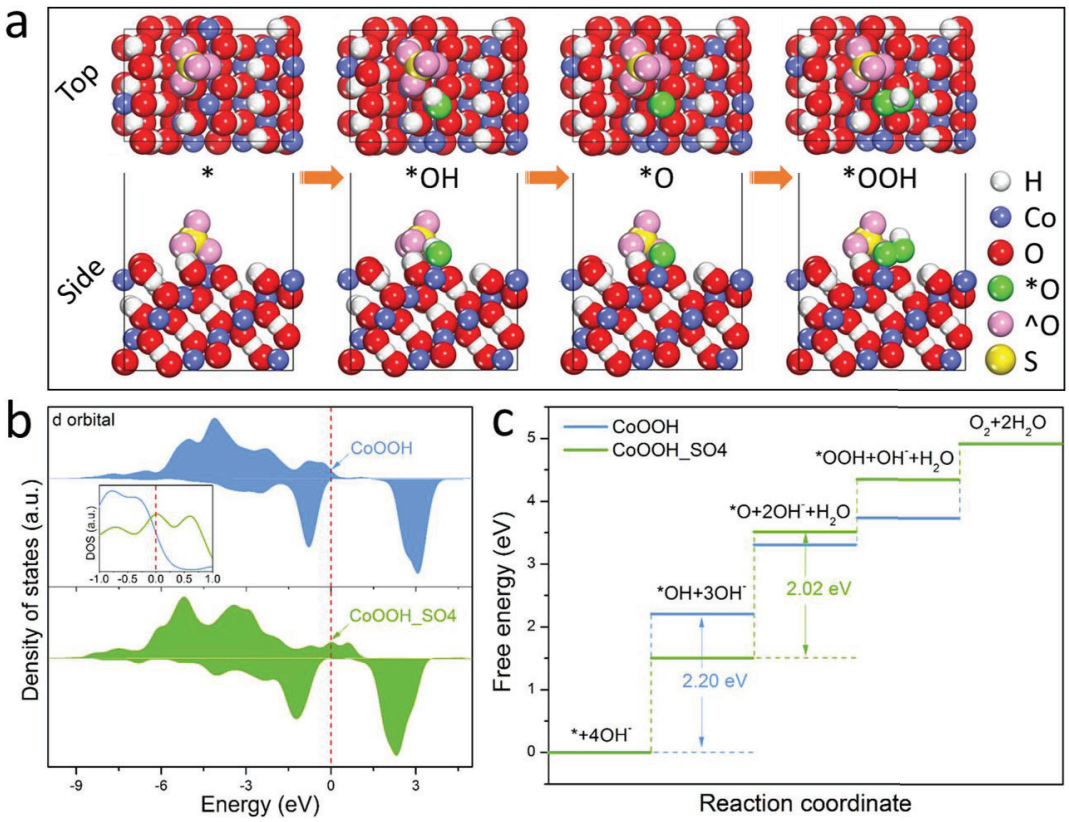

Figure 7. a) Optimized structural models of CoOOH-SO_4 for different OER steps. White balls represent hydrogen atoms, blue balls is cobalt atoms, and yellow balls stands for sulfur atoms, red ball represent the oxygen in the catalyst structure; green ball is the oxygen adsorbed on the intermediate; pink ball is the oxygen on the sulfate group. b) DOS of CoOOH and CoOOH-SO_4 regarding the Co 3d orbitals. c) Gibbs free energy diagrams of OER intermediates over CoOOH and CoOOH-SO_4.

4. Conclusions

In summary, the influence of several counterions on the structural, chemical and functional properties of $ZnCo_{1.23}Ni_{0.73}O_x$ electrocatalyst was analyzed. Materials were produced via a facile etching and annealing methods using ZIF-8 as a self-sacrificial template. $ZnCo_{1.23}Ni_{0.73}O_x$-SO_4 displayed excellent OER performances, including a low Tafel slope of 41.6 mV dec^{-1}, a very small overpotential of 252 mV for 10 mA cm^{-2}, and high stability during 100 h continuous operation. The high OER activity is associated with several factors, including the presence of oxygen vacancies, zinc leaching and the presence of sulfate anions. CV, I-T, XPS and EPR results indicate the simultaneous leaching of Zn, formation of oxygen vacancies and electrochemical surface reconstruction to CoOOH active species. DFT calculations proved that the decorated

SO_4^{2-} facilitates the formation of OOH* on CoOOH active sites, thus accelerating the OER process.

Acknowledgements

The authors thank the support from the projects COMBENERGY (PID2019-105490RB-C32) from the Spanish Ministerio de Ciencia e Innovación, ENE2016-77798-C4-3-R and NANOGEN (PID2020-116093RB-C43) funded by MCIN/AEI/10.13039/501100011033/ and by "ERDF A way of making Europe", by the "European Union". X. W., X. H. and R. D. thank the China Scholarship Council (CSC) for the scholarship support. The authors acknowledge funding from Generalitat de Catalunya 2017 SGR 327 and 2017 SGR 1246. ICN2 acknowledges the Severo Ochoa program from Spanish MINECO (Grant No. SEV-2017-0706). IREC and ICN2 are funded by the CERCA Programme /Generalitat de Catalunya. Z. L. acknowledges funding from MINECO SO-FPT PhD grant (SEV-2013-0295-17-1). Li is grateful for the project No.22NSFSC0966 provided by the Science & Technology Department of Sichuan Province. J.L. is a Serra Húnter Fellow and is grateful to MICINN/FEDER RTI2018-093996-B-C31, GC 2017 SGR 128 and ICREA Academia program. Part of the present work has been performed in the frameworks of Universitat de Barcelona Nanoscience PhD program and Universitat Autònoma de Barcelona Materials Science PhD program.

References

[1] J. Song, C. Wei, Z.F. Huang, C. Liu, L. Zeng, X. Wang, Z.J. Xu, A review on fundamentals for designing oxygen evolution electrocatalysts, Chem Soc Rev, 49 (2020) 2196-2214.

[2] J. Du, F. Li, L. Sun, Metal-organic frameworks and their derivatives as electrocatalysts for the oxygen evolution reaction, Chem Soc Rev, 50 (2021) 2663-2695.

[3] K. Wang, X. Wang, Z. Li, B. Yang, M. Ling, X. Gao, J. Lu, Q. Shi, L. Lei, G. Wu, Y. Hou, Designing 3d dual transition metal electrocatalysts for oxygen evolution reaction in alkaline electrolyte: Beyond oxides, Nano Energy, 77 (2020).

[4] L. Gao, X. Cui, C.D. Sewell, J. Li, Z. Lin, Recent advances in activating surface reconstruction for the high-efficiency oxygen evolution reaction, Chem Soc Rev, 50 (2021) 8428-8469.

[5] Z.P. Wu, X.F. Lu, S.Q. Zang, X.W. Lou, Non-Noble-Metal-Based Electrocatalysts toward the Oxygen Evolution Reaction, Adv. Funct. Mater, 30 (2020).

[6] M. Yu, E. Budiyanto, H. Tuysuz, Principles of Water Electrolysis and Recent Progress in Cobalt-, Nickel-, and Iron-Based Oxides for the Oxygen Evolution Reaction, Angew. Chem. Int. Ed, 61 (2022) e202103824.

[7] H. Wang, K.H. Zhang, J.P. Hofmann, A. Victor, F.E. Oropeza, The electronic structure of transition metal oxides for oxygen evolution reaction, J. Mater. Chem. A 9 (2021) 19465-19488.

[8] H. Wang, J. Li, K. Li, Y. Lin, J. Chen, L. Gao, V. Nicolosi, X. Xiao, J.M. Lee, Transition metal nitrides for electrochemical energy applications, Chem Soc Rev, 50 (2021) 1354-1390.

[9] A.K. Tareen, G.S. Priyanga, K. Khan, E. Pervaiz, T. Thomas, M. Yang, Nickel-based transition metal nitride electrocatalysts for the oxygen evolution reaction, ChemSusChem, 12 (2019) 3941-3954.

[10] J. Xu, J. Li, D. Xiong, B. Zhang, Y. Liu, K.H. Wu, I. Amorim, W. Li, L. Liu, Trends in activity for the oxygen evolution reaction on transition metal (M = Fe, Co, Ni) phosphide pre-catalysts, Chem Sci, 9 (2018) 3470-3476.

[11] A. Parra-Puerto, K.L. Ng, K. Fahy, A.E. Goode, M.P. Ryan, A. Kucernak, Supported Transition Metal Phosphides: Activity Survey for HER, ORR, OER, and Corrosion Resistance in Acid and Alkaline Electrolytes, ACS Catalysis, 9 (2019) 11515-11529.

[12] C. Wang, W. Chen, D. Yuan, S. Qian, D. Cai, J. Jiang, S. Zhang, Tailoring the nanostructure and electronic configuration of metal phosphides for efficient electrocatalytic oxygen evolution reactions, Nano Energy, 69 (2020) 104453.

[13] X. Wu, H. Zhang, J. Zhang, X.W.D. Lou, Recent Advances on Transition Metal Dichalcogenides for Electrochemical Energy Conversion, Adv Mater, 33 (2021) e2008376.

[14] J. Yin, J. Jin, H. Lin, Z. Yin, J. Li, M. Lu, L. Guo, P. Xi, Y. Tang, C.H. Yan, Optimized Metal Chalcogenides for Boosting Water Splitting, Adv。 Sci, 7 (2020) 1903070.

[15] S. Jin, Are Metal Chalcogenides, Nitrides, and Phosphides Oxygen Evolution Catalysts or Bifunctional Catalysts?, ACS Energy Letters, 2 (2017) 1937-1938.

[16] Y. Liu, X. Luo, C. Zhou, S. Du, D. Zhen, B. Chen, J. Li, Q. Wu, Y. Iru, D. Chen, A modulated electronic state strategy designed to integrate active HER and OER components as hybrid heterostructures for efficient overall water splitting, Appl. Catal. B, 260 (2020).

[17] X. Gu, Z. Liu, M. Li, J. Tian, L. Feng, Surface structure regulation and evaluation of FeNi-based nanoparticles for oxygen evolution reaction, Appl. Catal. B,, 297 (2021).

[18] H. Liao, T. Luo, P. Tan, K. Chen, L. Lu, Y. Liu, M. Liu, J. Pan, Unveiling Role of Sulfate Ion in Nickel-Iron (oxy)Hydroxide with Enhanced Oxygen-Evolving Performance, Adv. Funct. Mater. 31 (2021).

[19] C.F. Li, J.W. Zhao, L.J. Xie, J.Q. Wu, Q. Ren, Y. Wang, G.R. Li, Surface-Adsorbed Carboxylate Ligands on Layered Double Hydroxides/Metal-Organic Frameworks Promote the Electrocatalytic Oxygen Evolution Reaction, Angew. Chem. Int. Ed, 60 (2021) 18129-18137.

[20] R. Zhang, L. Wang, L. Pan, Z. Chen, W. Jia, X. Zhang, J.-J. Zou, Solid-acid-mediated electronic structure regulation of electrocatalysts and scaling relation breaking of oxygen evolution reaction, Appl. Catal. B,, 277 (2020).

[21] Y. Shi, W. Du, W. Zhou, C. Wang, S. Lu, S. Lu, B. Zhang, Unveiling the Promotion of Surface-Adsorbed Chalcogenate on the Electrocatalytic Oxygen Evolution Reaction, Angew. Chem. Int. Ed., 59 (2020) 22470-22474.

[22] S. Li, Z. Li, R. Ma, C. Gao, L. Liu, L. Hu, J. Zhu, T. Sun, Y. Tang, D. Liu, J. Wang, A Glass-Ceramic with Accelerated Surface Reconstruction toward the Efficient Oxygen Evolution Reaction, Angew. Chem. Int. Ed, 60 (2021) 3773-3780.

[23] Y. Zuo, Y. Liu, J. Li, R. Du, X. Han, T. Zhang, J. Arbiol, N.J. Divins, J. Llorca, N.J.C.o.m. Guijarro, In situ electrochemical oxidation of Cu_2S into CuO nanowires as a durable and efficient electrocatalyst for oxygen evolution reaction, Chem. Mater. 31 (2019) 7732-7743.

[24] G. Chen, Y. Zhu, H.M. Chen, Z. Hu, S.F. Hung, N. Ma, J. Dai, H.J. Lin, C.T. Chen, W. Zhou, Z. Shao, An Amorphous Nickel-Iron-Based Electrocatalyst with Unusual Local Structures for Ultrafast Oxygen Evolution Reaction, Adv Mater, 31 (2019) e1900883.

[25] J. Liu, Y. Ji, J. Nai, X. Niu, Y. Luo, L. Guo, S. Yang, Ultrathin amorphous cobalt–vanadium hydr(oxy)oxide catalysts for the oxygen evolution reaction, Energy Environ. Sci, 11 (2018) 1736-1741.

[26] S. Anantharaj, S. Noda, Amorphous catalysts and electrochemical water splitting: an untold story of harmony, Small, 16 (2020) 1905779.

[27] J. Kwon, H. Han, S. Jo, S. Choi, K.Y. Chung, G. Ali, K. Park, U. Paik, T. Song, Amorphous Nickel–Iron Borophosphate for a Robust and Efficient Oxygen Evolution Reaction, Adv. Energy Mater. 11 (2021).

[28] X. Li, L. Xiao, L. Zhou, Q. Xu, J. Weng, J. Xu, B. Liu, Adaptive bifunctional electrocatalyst of amorphous CoFe oxide@ 2D black phosphorus for overall water splitting, Angew. Chem. Int. Ed. 132 (2020) 21292-21299.

[29] X. Wang, C. Xing, Z. Liang, P. Guardia, X. Han, Y. Zuo, J. Llorca, J. Arbiol, J. Li, A. Cabot, Activating the lattice oxygen oxidation mechanism in amorphous molybdenum cobalt oxide nanosheets for water oxidation, J. Mater. Chem. A, (2022).

[30] H. Meng, W. Xi, Z. Ren, S. Du, J. Wu, L. Zhao, B. Liu, H. Fu, Solar-boosted electrocatalytic oxygen

evolution via catalytic site remodelling of CoCr layered double hydroxide, Appl. Catal. B, 284 (2021).

[31] Z.J. Chen, T. Zhang, X.Y. Gao, Y.J. Huang, X.H. Qin, Y.F. Wang, K. Zhao, X. Peng, C. Zhang, L. Liu, M.H. Zeng, H.B. Yu, Engineering Microdomains of Oxides in High-Entropy Alloy Electrodes toward Efficient Oxygen Evolution, Adv Mater, 33 (2021) e2101845.

[32] J. Bai, J. Mei, T. Liao, Q. Sun, Z.G. Chen, Z. Sun, Molybdenum-Promoted Surface Reconstruction in Polymorphic Cobalt for Initiating Rapid Oxygen Evolution, Adv. Energy Mater, 12 (2021).

[33] J. Zhang, T. Quast, W. He, S. Dieckhöfer, J.R. Junqueira, D. Öhl, P. Wilde, D. Jambrec, Y.T. Chen, W. Schuhmann, In-situ Carbon Corrosion and Cu Leaching as a Strategy for Boosting Oxygen Evolution Reaction in multi-metal Electrocatalysts, Adv Mater (2022) 2109108.

[34] S. Wahl, S.M. El-Refaei, A.G. Buzanich, P. Amsalem, K.s. Lee, N. Koch, M.L. Doublet, N. Pinna, Zn0. 35Co0. 65O–A stable and highly active oxygen evolution catalyst formed by zinc leaching and tetrahedral coordinated cobalt in wurtzite structure, Adv. Energy Mater. 9 (2019) 1900328.

[35] X.F. Lu, Y. Fang, D. Luan, X.W.D. Lou, Metal–organic frameworks derived functional materials for electrochemical energy storage and conversion: a mini review, Nano letters, 21 (2021) 1555-1565.

[36] M. Yang, C.H. Zhang, N.W. Li, D.Y. Luan, L. Yu, X.W. Lou, Design and Synthesis of Hollow Nanostructures for Electrochemical Water Splitting, Adv. Sci., (2022) 2105135.

[37] W. Wang, H. Yan, U. Anand, U.J.J.o.t.A.C.S. Mirsaidov, Visualizing the conversion of metal–organic framework nanoparticles into hollow layered double hydroxide nanocages, J. Am. Chem. Soc 143 (2021) 1854-1862.

[38] W. Cheng, Z.P. Wu, D. Luan, S.Q. Zang, X.W. Lou, Synergetic Cobalt-Copper-Based Bimetal–Organic Framework Nanoboxes toward Efficient Electrochemical Oxygen Evolution, Angew. Chem. Int. Ed, 60 (2021) 26397-26402.

[39] Y. Huang, S.L. Zhang, X.F. Lu, Z.P. Wu, D. Luan, X.W.D. Lou, Trimetallic Spinel $NiCo_{2-x}Fe_xO_4$ Nanoboxes for Highly Efficient Electrocatalytic Oxygen Evolution, Angew Chem Int Ed Engl, 60 (2021) 11841-11846.

[40] C. Qiao, Z. Usman, T. Cao, S. Rafai, Z. Wang, Y. Zhu, C. Cao, J. Zhang, High-valence Ni and Fe sites on sulfated NiFe-LDH nanosheets to enhance O-O coupling for water oxidation, Chem. Eng. J. 426 (2021).

[41] N.V. Chukanov, A.D. Chervonnyi, Infrared spectroscopy of minerals and related compounds, Springer2016.

[42] G. Wu, X. Zheng, P. Cui, H. Jiang, X. Wang, Y. Qu, W. Chen, Y. Lin, H. Li, X. Han, A general synthesis approach for amorphous noble metal nanosheets, Nat. Commun, 10 (2019) 1-8.

[43] C.C. McCrory, S. Jung, J.C. Peters, T.F.J.J.o.t.A.C.S. Jaramillo, Benchmarking heterogeneous electrocatalysts for the oxygen evolution reaction, J. Am. Chem. Soc. 135 (2013) 16977-16987.

[44] S.L. Zhang, B.Y. Guan, X.F. Lu, S. Xi, Y. Du, X.W.D. Lou, Metal Atom-Doped Co_3O_4 Hierarchical Nanoplates for Electrocatalytic Oxygen Evolution, Adv Mater, 32 (2020) e2002235.

[45] Z.-F. Huang, J. Song, Y. Du, S. Xi, S. Dou, J.M.V. Nsanzimana, C. Wang, Z.J. Xu, X. Wang, Chemical and structural origin of lattice oxygen oxidation in Co–Zn oxyhydroxide oxygen evolution electrocatalysts, Nat. Energy 4 (2019) 329-338.

[46] M. Fang, D. Han, W.B. Xu, Y. Shen, Y. Lu, P. Cao, S. Han, W. Xu, D. Zhu, W. Liu, Surface-guided formation of amorphous mixed-metal oxyhydroxides on ultrathin MnO2 nanosheet arrays for efficient electrocatalytic oxygen evolution, Adv. Energy Mater. 10 (2020) 2001059.

[47] S.Y. Lim, S. Park, S.W. Im, H. Ha, H. Seo, K.T. Nam, Chemically deposited amorphous Zn-doped NiFeO x H y for enhanced water oxidation, ACS Catal., 10 (2019) 235-244.

[48] Y. Duan, S. Sun, Y. Sun, S. Xi, X. Chi, Q. Zhang, X. Ren, J. Wang, S.J.H. Ong, Y. Du, L. Gu, A. Grimaud, Z.J. Xu, Mastering Surface Reconstruction of Metastable Spinel Oxides for Better Water Oxidation, Adv Mater, 31 (2019) e1807898.

[49] T. Ling, T. Zhang, B. Ge, L. Han, L. Zheng, F. Lin, Z. Xu, W.B. Hu, X.W. Du, K. Davey, S.Z. Qiao, Well-Dispersed Nickel- and Zinc-Tailored Electronic Structure of a Transition Metal Oxide for Highly Active Alkaline Hydrogen Evolution Reaction, Adv Mater, 31 (2019) e1807771.

[50] Y. Sun, X. Ren, S. Sun, Z. Liu, S. Xi, Z.J. Xu, Engineering High-Spin State Cobalt Cations in Spinel Zinc Cobalt Oxide for Spin Channel Propagation and Active Site Enhancement in Water Oxidation, Angew. Chem. Int. Ed, 60 (2021) 14536-14544.

[51] A. Bergmann, T.E. Jones, E. Martinez Moreno, D. Teschner, P. Chernev, M. Gliech, T. Reier, H. Dau, P. Strasser, Unified structural motifs of the catalytically active state of Co (oxyhydr) oxides during the electrochemical oxygen evolution reaction, Nat. Catal., 1 (2018) 711-719.

[52] J. He, X. Zhou, P. Xu, J. Sun, Promoting electrocatalytic water oxidation through tungsten-modulated oxygen vacancies on hierarchical FeNi-layered double hydroxide, Nano Energy, 80 (2021) 105540.

[53] L. Zhang, C. Lu, F. Ye, Z. Wu, Y. Wang, L. Jiang, L. Zhang, C. Cheng, Z. Sun, L. Hu, Vacancies boosting strategy enabling enhanced oxygen evolution activity in a library of novel amorphous selenite electrocatalysts, Appl. Catal. B, 284 (2021).

[54] D. Guan, G. Ryu, Z. Hu, J. Zhou, C.L. Dong, Y.C. Huang, K. Zhang, Y. Zhong, A.C. Komarek, M. Zhu, X. Wu, C.W. Pao, C.K. Chang, H.J. Lin, C.T. Chen, W. Zhou, Z. Shao, Utilizing ion leaching effects for achieving high oxygen-evolving performance on hybrid nanocomposite with self-optimized behaviors, Nat Commun, 11 (2020) 3376.

[55] R.I. Sayler, B.M. Hunter, W. Fu, H.B. Gray, R.D. Britt, EPR spectroscopy of iron-and nickel-doped [ZnAl]-layered double hydroxides: Modeling active sites in heterogeneous water oxidation catalysts, J. Am. Chem. Soc., 142 (2019) 1838-1845.

[56] J. Wang, J. Liu, B. Zhang, F. Cheng, Y. Ruan, X. Ji, K. Xu, C. Chen, L. Miao, J. Jiang, Stabilizing the oxygen vacancies and promoting water-oxidation kinetics in cobalt oxides by lower valence-state doping, Nano Energy, 53 (2018) 144-151.

[57] W. Xu, W. Gao, L. Meng, W. Tian, L. Li, Incorporation of Sulfate Anions and Sulfur Vacancies in ZnIn2S4 Photoanode for Enhanced Photoelectrochemical Water Splitting, Adv. Energy Mater, 11 (2021).

Graphical Abstract

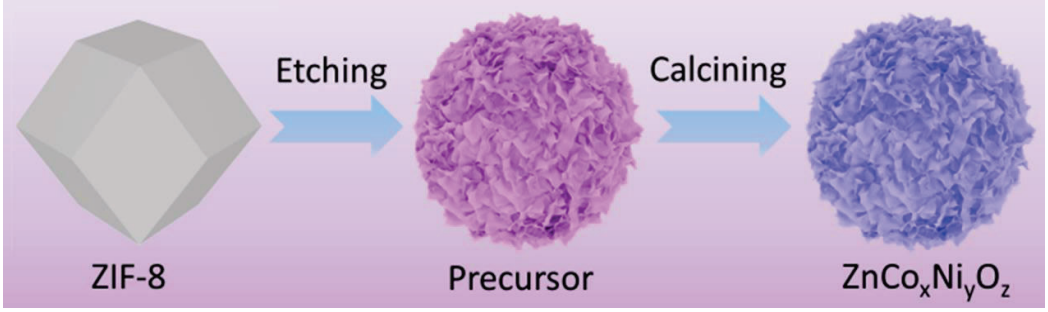

Different anionic groups decorated $ZnCo_xNi_yO_z$ nanosheets are produced by a facile proton etching and ion exchange method used ZIF-8 as templates. Unveiling the role of counter-anions on electrocatalyst performance. Oxygen defects caused by zinc leaching and the presence of sulfate anions improved the OER activity.